

**Contactless generation of cavitation in high temperature liquid metals and its impact on particle dispersion in solidified iron and steel samples**

Sarma, M.; Grants, I.; Herrmannsdörfer, T.; Gerbeth, G.;

Originally published:

May 2021

**Journal of Materials Processing Technology 291(2021), 117041**

DOI: <https://doi.org/10.1016/j.jmatprot.2021.117041>

Perma-Link to Publication Repository of HZDR:

<https://www.hzdr.de/publications/Publ-32074>

Release of the secondary publication  
on the basis of the German Copyright Law § 38 Section 4.

CC BY-NC-ND

# Contactless generation of cavitation in high temperature liquid metals and its impact on particle dispersion in solidified iron and steel samples

Mārtiņš Sarma <sup>a\*</sup>, Ilmārs Grants <sup>b</sup>, Thomas Herrmannsdörfer <sup>c</sup>, Gunter Gerbeth <sup>a</sup>

<sup>a</sup> Institute of Fluid Dynamics, Helmholtz-Zentrum Dresden - Rossendorf, Bautzner Landstraße 400, 01328 Dresden, Germany

<sup>b</sup> Institute of Physics, University of Latvia, Miera iela 32, LV-2169 Salaspils, Latvia

<sup>c</sup> Dresden High Magnetic Field Laboratory, Helmholtz-Zentrum Dresden - Rossendorf, Bautzner Landstraße 400, 01328 Dresden, Germany

---

## Abstract

A recently developed method for the contactless magnetic generation of cavitation is demonstrated for high-melting-point metals. The approach is based on the floating-zone technique, which is truly contactless and crucible-free as it uses electromagnetic forces. Using this method, ultra-high-temperature ceramic particles, such as TiN, TiB<sub>2</sub> and TiC, are admixed in liquid iron and 316L steel. The dispersion and particle refinement caused by cavitation treatment during melting and solidification are investigated. Magnetic fields up to 8 T that correspond to pressure oscillation amplitude of 0.83 MPa are used. The signal emitted by the collapsing bubbles is captured and visualized for iron melts. Samples with a higher number of cavitation nuclei exhibit a more stable cavitation response. Improved reinforcement refinement is demonstrated for increasing cavitation intensity – the size of precipitates is evidently reduced due to the cavitation treatment.

**Keywords:** Metal matrix composites, Contactless cavitation, Solidification processing, Iron, Steel

---

## 1 Introduction

The addition of high modulus reinforcement to a metal matrix can significantly change the material properties and improve the mechanical qualities of the end product. This material class is termed metal matrix composites (MMCs). While the market share is dominated by light metals, two distinct and highly prospective steel composite groups exist. The proposed future nuclear energy systems (Generation IV), such as fusion reactors or the next generation of fission reactors, require new materials with improved creep strength at high temperatures and superior radiation resistance. As explained by Ukai and Fujiwara (2002), oxide dispersion strengthened (ODS) steels have the largest potential to offer the required properties due to the nano-sized oxide

---

\*Corresponding author

Email address: m.sarma@hzdr.de (Mārtiņš Sarma)

particles blocking the movement of mobile dislocations. The other important class is high modulus steel (HMS). To reach CO<sub>2</sub> emission targets, the transport industry is in a dire need of further optimization and reduction of weight while maintaining structural integrity. As illustrated by Bonnet et al. (2014), HMS can be an especially attractive class of materials to reach the desired mechanical properties by combining a ductile metallic matrix with stiff yet lower density ceramic particles.

Solid-state manufacturing is the predominant production route for MMCs. It consists of the initial powder preparation with gas atomization, blending, mechanical alloying in ball mills, canning and degassing, consolidating (hot-isostatic pressing, spark plasma sintering, etc.) and post-processing (hot or cold rolling, heat treatment, etc.). However, due to the many complex and expensive steps involved, it quickly becomes costly. Furthermore, upscaling to industrially required sizes, e.g. for nuclear power plants, is often limited, as reviewed by Bergner et al. (2016). Therefore, a simple casting route is a very attractive alternative. However, due to the usually unfavorable wetting of ceramic particles by liquid metal, the reinforcements tend to agglomerate and dispersion becomes a significant challenge. An efficient solution for this problem is ultrasonic treatment of the melt – the formation, expansion, pulsation and rapid collapse of bubbles within the liquid can create very extreme local conditions – “hot spots” as described by Fitzgerald et al. (1956). Suslick et al. (1999) have estimated that temperature in these regions can be as high as 5000 K, while the pressure can reach 1000 MPa and the cooling rate above  $10 \times 10^{10}$  K s<sup>-1</sup>. Besides the hot spots, the collapses produce high-speed jets in the range of 200–1000 m s<sup>-1</sup> with local impact pressures in the GPa range, as measured by Tzanakis et al. (2014). Li et al. (2019) have shown that these violent events are sufficiently strong to break particle agglomerates and improve wettability by breaking up the oxide layer usually covering liquid metals and forcing the melt inside crevices of solid surfaces.

The cavitation is traditionally induced by a piezoelectric transducer through a metallic or ceramic sonotrode immersed in the liquid metal. This approach has been proven to be effective, for example, by Lan et al. (2004), who have produced a SiC-reinforced Mg composite, and Liu et al. (2014), who demonstrated SiC and Al<sub>2</sub>O<sub>3</sub> particle dispersion in Al. In general, ultrasonic processing improves the mechanical properties of the material by evenly dispersing the particles and refining the microstructure, as demonstrated by Yuan et al. (2019). However, it is not possible to directly introduce cavitation in high-melting-point metals, such as iron or steel, simply because of the extreme conditions (high melting temperature and very reactive environment). Therefore, the contactless generation of acoustic cavitation in such melts is an important topic to facilitate ODS steel and HMS development.

Vivès (1996) was first to present the contactless generation of cavitation in liquid aluminum by applying a perpendicular steady magnetic field to a sine wave current. The product of the two fields gives rise to an oscillating electromagnetic force that generates a pressure in the melt that varies over time and is capable of producing cavitation. Henderson et al. (2014) proposed a similar concept to introduce compression waves into the melt, but using a steel crucible to contain the melt. Such approach is limited to light metals. A different technique has been presented by Bojarevics et al. (2015) using a two-coil system – the main coil is responsible for heating the melt while the secondary, adjustable coil is placed in the vicinity of the melt surface. A high-frequency current depresses the melt surface while also providing rapid melt vibration and cavitation. However, as of today none of these approaches have been successful in

processing high-melting-point metals due to the very extreme conditions associated with the reactive liquid metal environment and the rapid decay of crucibles, facilitated by intense cavitation activity. An approach for processing steel was proposed by Grants et al. (2015) where a concept similar to floating-zone melting was used to investigate cavitation in light metals. Superimposing a steady magnetic field on the induced magnetic field generates pressure oscillations directly in the melt, while the floating-zone concept provides a truly contactless, crucible-free approach.

This paper advances the floating-zone melting technique and presents, to the best of our knowledge for the first time, a systematic comparison and results of successful particle dispersion in iron and steel using contactless cavitation treatment. The experiments are conducted using DC magnetic fields up to 8 T.

## 2 Experimental procedure

A selection of results will be presented with the particles listed in Table 1. TiC, for example, has been proposed by Terry and Chinyamakobvu (1992b) as an excellent reinforcement in iron alloys due to its good wetting properties. According to Ramqvist (1965), it is also considered one of the most stable carbides with a melting point around 3000 °C. An in-situ method for producing TiN-reinforced iron has already been successfully presented by Wang et al. (2010), while the sessile drop experiments conducted by Amadeh et al. (2001) reveal the nitride's good wettability and relatively low solubility in iron and steel. Lastly, TiB<sub>2</sub> has been successfully used as a reinforcement for in-situ HMS production by Springer et al. (2015). Furthermore, dispersion of the boride has also proven to be relatively good in iron, although reaction with carbon and the subsequent formation of TiC and Fe<sub>2</sub>B can take place, as demonstrated by Terry and Chinyamakobvu (1992a). In the present paper, the effect of cavitation for the dispersion of these ceramic particles was investigated in low-carbon stainless steel grade 1.4404 (AISI 316L; Fe-Cr18-Ni10-Mo3) and pure iron.

The high surface tension of liquid metals provides a challenge to insert the particles directly. As a solution, the particles are mixed together with the matrix powder and compressed into a small, electrically conducting tablet (concept similar to a master alloy). To investigate cavitation dependence on increased porosity and the proportion of inclusions, two different approaches are employed. The tablets are produced either by cold pressing or by spark plasma sintering (SPS) with a 12 kN force for 5 hours at 1120 °C in an Ar atmosphere. The created tablets have a diameter of 20 mm and thickness of around 5 mm. Ceramic particles amount to roughly 1–2 wt% per tablet.

Table 1. List of the investigated particles in the paper.

Compound	Particle size (μm)	Melting point (°C)	Density (g cm <sup>-3</sup> )
TiC	0.8	3200	4.93
TiN	0.8	2950	5.22
TiB <sub>2</sub>	2–6	2900	4.52

A sketch of the set-up is shown in Fig. 1. The initial tablet (1) consisting of the matrix material and reinforcement powder is placed between two supports (2) which are made of the required matrix material and are partly molten together with the tablet, creating a composite. The

conditions are similar to static floating-zone melting – the process is crucible-free and the melting zone is confined by the large surface tension of the melt and the magnetic pressure. To prevent excessive oxidation of the sample, the melting is done in 0.5–5 mbar Ar atmosphere, enclosed by a quartz tube (3) from the sides. Water-cooled copper plates (4) from the top and bottom provide some control over the solidification rate. An alternating current  $I_{AC} = 1300$  A at  $f = 14$  kHz frequency is applied to the sample using a 4-turn induction coil (5) that supports the melting of the sample. The pre-sonication melting of the composites is carried out for at least 10 minutes to facilitate the wetting of the particles by the liquid metal and to improve the dispersion. The maximum r.m.s. current corresponds to a roughly  $b_{AC} = 0.13$  T induced magnetic field in the center of the coil.

When assembled, the set-up is positioned in a static magnetic field  $B_{DC}$  provided either by an electromagnet or a superconducting wide-bore (150 mm) high-field (maximum 19 T) magnet system at the Dresden High Magnetic Field Laboratory (HLD-EMFL). The simultaneous application of AC and DC magnetic fields creates electromagnetic vibrations in the volume that may lead to cavitation. Piezo elements (6) which record sound emitted by the cavitation are placed in grooves that are machined into the shielding plates. The sample is sonicated for at least 30 minutes with all other parameters remaining constant, then solidified under the action of the oscillating force by slowly lowering the power. To prevent the evaporation of helium in a superconducting magnet system, a multi-walled chamber is used. This consists of an inner copper tube (7) for shielding the superconducting magnet coils from induction currents and an outer stainless steel tube (8) which acts as a separator between the coolant and the copper tube. A vacuum is used for thermal insulation between the inner and outer layers of the chamber.

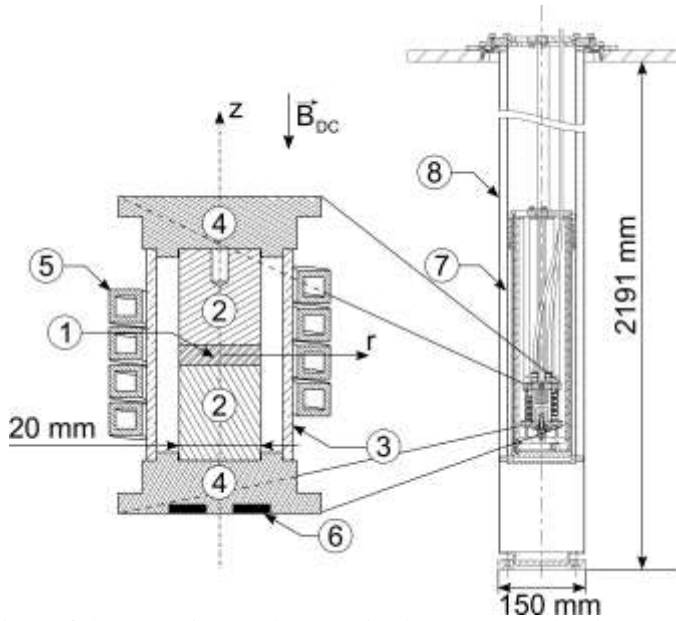


Fig. 1. Schematic view of the experimental set-up in the superconducting magnet system: (1) tablet containing the powder and matrix mixture, (2) supports from the matrix material, (3) quartz tube, (4) water cooled copper shielding plates, (5) induction coil, (6) position of the piezo elements, (7) inner shielding tube from copper, (8) outer stainless steel tube with vacuum in-between; the melting chamber is positioned in the center of the superconducting coils.

The samples produced with the contactless cavitation treatment are, on average, 30 mm long with a diameter of 20 mm. As the particles are released into a larger volume, after the melting the composite consists of around 0.2 wt% reinforcement phase. The samples are cut in half and the molten region is extracted. The specimen is then mounted using cold mounting resin, and ground and polished using increasingly finer abrasives. The samples presented in this paper are taken from the middle of the specimen and have characteristics typical of the whole volume. Microstructures are characterized with an optical light microscope (LM; Leica DM6000 M) and scanning electron microscope (SEM; Zeiss EVO 50) for secondary electron (SE) and back-scattered electron (BSE) imaging. Elemental analysis is performed using energy-dispersive X-ray spectroscopy (EDS; Bruker AXS XFlash detector 4010).

### 3 Theoretical analysis

By the most basic definition of cavitation the liquid must be torn apart, creating cavities or voids in the liquid which then fill with vapor and/or gas. In an ideal case, the tension required is equal to the tensile strength of the liquid; in reality, impurities act as weak points (and cavitation nuclei) which lower the necessary strength. To generate tension in the liquid, for some part of the oscillation cycle the oscillating pressure amplitude  $P_A$  must be greater than the ambient one to create a negative pressure inside the liquid. A minimum value for the acoustic pressure (the Blake threshold) must be reached to cause the explosive growth of a bubble with the initial radius  $R_B$  (the Blake radius). This is the lower threshold for transient cavitation, as explained by Leighton (1994), and is given by

$$P_A = p_0 + \frac{8\gamma}{9} \sqrt{\frac{3\gamma}{2R_B^3(p_0 + (2\gamma/R_B))}}, \quad (1)$$

where  $p_0$  is the ambient pressure and  $\gamma$  is the surface tension. In the experiments, the ambient pressure is in the order of 500 Pa, and is thus negligible.

Taking the surface tension of liquid iron as  $1.872 \text{ N m}^{-1}$  and estimating the minimum cavitating bubble size as similar to the size of  $\text{TiB}_2$  particles from Table 1, the minimum required acoustic pressure for the explosive growth of such bubbles is  $P_A = 0.72 \text{ MPa}$ . Now the question arises whether such pressure amplitude can be obtained with the contactless magnetic approach. For the case considered in this work, the attainable oscillating pressure amplitude is limited by the experimental configuration, namely the electromagnetic force due to the induced AC and the static DC magnetic fields.

The irrotational part of this force creates an oscillating pressure field while the rotational part drives an oscillating liquid motion. To estimate the achievable pressure amplitude, a simplified model can be considered. A cylindrical volume of liquid metal with an electric conductivity  $\sigma$ , height  $2z_0$  and radius  $r_0$  is bounded from the top and bottom by semi-infinite solid non-magnetic cylinders (this property is fulfilled here as the Curie temperature is always exceeded during melting) with the same electrical conductivity and radius. The cylinder is placed in a magnetic field with steady and oscillating axial components

$$\mathbf{B}(r, z, t) = B_{DC}\mathbf{e}_z + \nabla \times [\mathbf{e}_\phi A(r, z)] e^{i\omega t}, \quad (2)$$

where  $t$  denotes time,  $\omega$  is the angular frequency and  $\mathbf{e}_z$  and  $\mathbf{e}_\phi$  are the unit vectors in the axial and azimuthal directions. The complex vector potential is expressed by the infinite cylinder solution

extended by an appropriate modeling of the axial dependency, as defined by Grants and Gerbeth (2018)

$$A(r, z) = \frac{b_{AC} r_0}{\sqrt{iS}} \frac{I_1\left(\sqrt{iS} \frac{r}{r_0}\right)}{I_0\left(\sqrt{iS}\right)} \left(1 - \varepsilon \left(\frac{z}{z_0}\right)^2\right), \quad (3)$$

where  $\varepsilon$  is the deviation from a uniform distribution of the alternating magnetic field and  $S$  is the shielding factor  $S = \omega \sigma \mu_0 r_0^2$ .  $I_0$  and  $I_1$  are the modified Bessel functions of the first kind. Lastly,  $b_{AC}$  denotes the alternating magnetic field induction amplitude on the cylinder surface at mid-height  $z = 0$ . Then, the induced current density amplitude can be expressed as  $j_\phi(r, z) = -i\sigma\omega A(r, z)$ . The current in combination with a steady axial field  $B_{DC}\mathbf{e}_z$  produces an oscillating radial body force

$$\mathbf{F}_{osc}(r, z, t) = B_{DC}\mathbf{e}_z \times j_\phi(r, z)\mathbf{e}_\phi e^{i\omega t}. \quad (4)$$

As shown by Grants et al. (2015), in the theoretical case of an infinite cylinder, i.e.  $\varepsilon = 0$ , the force is purely irrotational and allows for an analytical solution. For  $S \gg 1$  the pressure oscillation amplitude is simply given as

$$P_A = \frac{B_{DC} b_{AC}}{\mu_0}. \quad (5)$$

As  $r_0$  is much smaller than the acoustic wavelength, the oscillating pressure field  $p'$  can be calculated from the Navier–Stokes equation by fully decoupling the velocity field into the base flow  $\mathbf{v}$  and the oscillating flow  $\mathbf{v}'$  with  $\omega$  as the driving frequency. Then the equation for  $\mathbf{v}'$  and  $p'$  may be written as

$$\rho \frac{\partial \mathbf{v}'}{\partial t} = \eta \nabla^2 \mathbf{v}' - \nabla p' + \mathbf{F}_{osc}, \quad (6)$$

where  $\rho$  is the density and  $\eta$  the viscosity of the liquid metal. Outside the viscous boundary layer, which has a characteristic thickness  $(\eta/\rho\omega)^{1/2}$  of a few micrometers in the case discussed here, the diffusion term can be removed from (6). Taking the divergence produces a simplified equation for the pressure amplitude

$$\nabla^2 p' = \nabla \cdot \mathbf{F}_{osc}. \quad (7)$$

This equation is solved numerically by a finite element method with Wolfram Mathematica. A zero pressure amplitude condition is applied on the free surface  $r = r_0$  and a zero normal derivative boundary condition is applied at the symmetry axis and at the top liquid-solid interface of the cylinder ( $z = z_0$ ). Furthermore, the variation of the magnetic field is taken as  $\varepsilon = 0.1$ , which is reasonably fulfilled for a short coil with a liquid metal part with dimensions of  $r_0 = z_0$ . Fig. 2 shows the electromagnetic oscillating force (a) and the pressure amplitude distribution (b) for the real experimental conditions with an iron sample in an alternating magnetic field of  $S = 110$  with  $b_{AC} = 0.13$  T,  $r_0, z_0 = 10$  mm and  $B_{DC} = 8$  T. The pressure amplitude gradually increases over the skin depth, reaching a maximum at a distance of twice the skin layer, followed by a slight decrease and stabilization over the rest of the volume. Most importantly, it can be seen that the necessary Blake's critical threshold calculated previously,  $P_A = 0.72$  MPa, is comfortably achieved throughout the volume of the sample, providing cavitation conditions throughout the liquid phase. Using  $B_{DC} = 8$  T, the maximum oscillating pressure amplitude reaches  $P_A \approx 0.85$  MPa in this case.

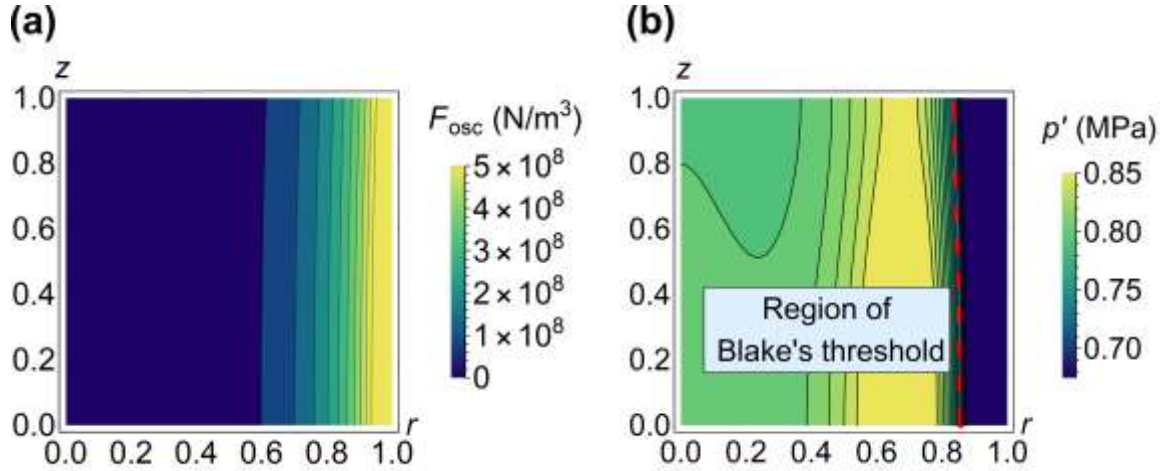


Fig. 2. Isolines of the electromagnetic oscillating force  $F_{osc}$  amplitude (a) and pressure  $p'$  amplitude distribution (b) in a cylindrical sample at  $S = 110$ . The region with  $P_A \geq 0.72$  MPa is marked by the red dashed line. The dimensions are scaled by  $r_0$  and  $z_0$ .

In combination with the alternating magnetic field, the induced current also creates a force driving the typical flow of two counter-rotating tori. In addition, from (6) it follows that a rapidly oscillating flow arises. Averaged over time it is zero, yet the induced shear stresses may contribute to the mean flow in a form of acoustic streaming. However, a significant flow damping is also expected due to the applied steady magnetic field. The MHD interaction parameter

$$N = \frac{\sigma B_{DC}^2 L}{\rho u} \quad (8)$$

is much larger than unity in the case of 8 T, which implies that the flow braking force dominates over the inertia. The characteristic velocity  $u$  at high magnetic fields can be expressed as in Grants and Gerbeth (2018), where scaling with  $O(\text{Ha}^{-3/2})$  was identified (Ha is the Hartmann number). In the case of 8 T, the maximum flow velocity can reach around  $2 \text{ cm s}^{-1}$ . While such flow is relatively slow, over the length of experiment the mixing time  $T_{\text{exp}}$  is much longer than the period of one vortex  $\tau = r_0/u$ . Therefore, sufficient mass homogenization is expected.

## 4 Results and discussion

### 4.1 Cavitation detection

Cavitating bubbles emit acoustic waves, which can be analyzed and used to characterize the cavitation. This has been demonstrated by various authors (Cramer and Lauterborn, 1982; Ilyichev et al., 1989; Tzanakis et al., 2016). The spectrum of cavitation noise consists of a variety of harmonics ( $n f_0$ ,  $n = 2, 3\dots$ ), sub-harmonics ( $f_0/m$ ,  $m = 2, 3\dots$ ) and ultra-harmonics ( $n f_0/m$ ,  $n = 2, 3\dots$  and  $m = 2, 3\dots$ ) of the fundamental driving frequency  $f_0$ . Furthermore, a broadband continuum (background white noise) is present, which becomes more pronounced when approaching the transient threshold. At low excitation power, a cavitating bubble emits sound at  $f_0$ . At a higher acoustic pressure, but below the transient threshold, harmonics at  $n = 2, 3\dots$  appear. Lastly, the onset of the transient cavitation is marked by broadening of the spectral lines, a major increase in broadband noise and the appearance of sub and ultra-harmonics. This emitted acoustic signal is recorded using ceramic piezoelectric sensors (Ferroperm; Pz27) with a 4 MHz

resonant frequency. These are attached to the copper shielding plates. The electric signal is measured with a digital oscilloscope (Tektronix DPO7104). Two channels are devoted to cavitation signal measurements while two others are used to measure the supplied voltage with a differential probe (Tektronix TMDP0200) and the current with a Rogowski coil (PEM CWT3LFB). The signal is acquired in packets of 5000 measurements with a sampling rate of 312.5 kHz and transferred to the workstation once a second.

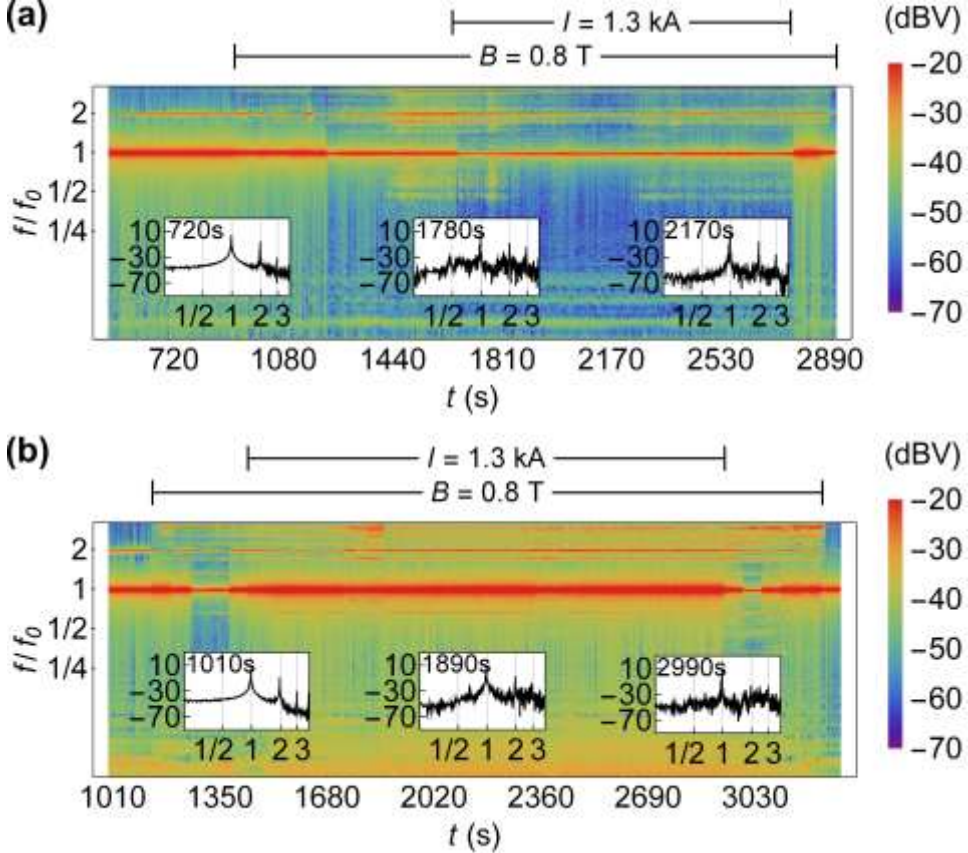


Fig. 3. (a) Cavitation spectrum from the processing of pure iron with  $0.8 \mu\text{m}$  TiC. Initial sample is produced with SPS. The inset at 720 seconds shows the spectrum without the static magnetic field. A magnetic field,  $B_{DC} = 0.8 \text{ T}$ , is applied from 920 to 2910 seconds. The maximum current is applied from 1640 to 2760 seconds. A slight broadening of the spectrum from 1440 to 1810 seconds is observable in the inset at 1780 seconds, then again from 2200 seconds on. During the gap, there are no signs of cavitation, as shown in the inset at 2170 seconds. The broad low-frequency part includes a wide  $f_0/2$  peak. (b) Cavitation spectrum from the processing of pure iron with  $0.8 \mu\text{m}$  TiC. Initial sample is produced without SPS. The inset at 1010 seconds shows the spectrum without the static magnetic field. A magnetic field,  $B_{DC} = 0.8 \text{ T}$ , is applied from 1140 to 3240 seconds. The maximum current is applied from 1440 to 2940 seconds. The inset at 1890 seconds shows a strong  $2f_0/3$  peak, which becomes weaker near the end of the processing. Possibly, a dim  $f_0/2$  exists within the background noise, as can be seen in the inset at 2990 seconds.

To find the power spectrum, the measured voltage from the piezo element is transformed to the frequency domain using the discrete Fourier transform. Plotting all of the obtained spectra

versus time creates a two-dimensional image showing the dynamics of the recorded sound signal and thus the cavitation throughout the experiment. Fig. 3 presents a representative set of results obtained with an acoustic pressure oscillation amplitude of around 80 kPa, with and without sintering of the initial tablets (Fe/TiC).

The spectrum from processing iron with 0.8  $\mu\text{m}$  TiC particles (initial sample created by SPS) can be seen in Fig. 3 (a). The given spectra are limited to the time frame when the initial tablet can be considered fully molten together with the sample holders. A static magnetic field of 0.8 T is applied from 920 to 2910 seconds. The maximum AC is 1300 A from 1640 to 2760 seconds. The first inset shows the recorded signal without cavitation treatment when the sample is already liquid. When the magnet is turned on, nothing changes in the low-frequency range; some weak peaks appear at higher harmonics. At around 1440 seconds there is a change in the signal: a sudden broadening of the spectrum in the low-frequency range can be observed. The inset at 1780 seconds, during maximum processing conditions, possibly reveals frail, but wide  $f_0/2$ . This broadening of the signal is not continuous, as quiet phases can be seen, e.g. in the 2170 seconds inset.

The spectrum from processing iron with an initial sample produced without SPS can be seen in Fig. 3 (b). A static magnetic field of 0.8 T is applied from 1140 to 3240 seconds. The maximum current is from 1440 to 2940 seconds. A stable  $2f_0/3$  peak can be observed throughout the experiment, as shown in the 1890 seconds inset. At around 2990 seconds, the low-frequency noise has increased, and a weak  $f_0/2$  possibly emerges, as shown in the inset.

As the only available information is the recorded sound emitted by many cavitating bubbles, it does not directly translate to the cavitation impact or strength. As such, any description is limited to comparison of the power level emitted by sound in different experiments. In the cases presented above, the noise level without the steady magnetic field is around -45 dBV. The processing of iron with a sintered initial sample has the shortest-lived cavitation activity with a  $f_0/2$  peak that reaches a maximum at -30 dBV, while exhibiting a sporadic response. Melting when the initial sample is simply cold-pressed creates a relatively stable  $2f_0/3$  peak for the whole duration of the experiment. However, a decrease can be observed from -20 dBV at the beginning to -25 dBV at the end.

The observable peaks indicate cavitation activity. Accordingly, 80 kPa can be considered the cavitation onset for iron. However, the experimentally determined threshold is below the theoretical value found earlier ( $P_A = 0.72$  MPa for iron), permitting weaker magnetic fields to be employed. The appearance of the cavitation arising from a lower magnetic field implies that larger bubbles are cavitating. According to equation (1), 83 kPa is sufficient to cavitate bubbles with a radius of 20  $\mu\text{m}$ . Since there are no free-floating gas bubbles in liquid iron, the inception may arise from various impurities and gas pockets around the added particles, which act as cavitation nuclei. Voids created at these weak points are quickly filled by the dissolved gas from the liquid due to rectified diffusion.

However, the infrequent and relatively subtle appearance in the spectra also indicates that the pressure amplitude is not high enough for full-scale cavitation. An improvement can be achieved by creating the conditions for resonance, given as (Eskin and Eskin, 2014)

$$\omega = \frac{1}{2\pi R_r} \sqrt{\frac{3\kappa}{\rho} \left( p_0 + \frac{3\gamma}{R_r} \right)} \quad (9)$$

where  $R_r$  is the resonance radius and  $\kappa$  is the polytropic exponent (5/3 for Ar). For an AC field frequency of 14 kHz, the resonance size of a bubble is 80  $\mu\text{m}$ . Otherwise, much more explosive growth could probably be achieved in a 20  $\mu\text{m}$  bubble with a field frequency of around 100 kHz.

Generally, the demonstrated comparison indicates that initial samples produced without sintering are more prone to initiate cavitation. A cold-pressed sample is likely to contain a higher amount of impurities: the processing temperatures are lower and production byproducts do not react, as the sample is not liquefied. Additionally, there is a larger quantity of entrapped gas inside the tablet which is released during melting. In other words, cold-pressed samples have many more cavitation nuclei that, together with the added ceramic reinforcement phase, facilitates the onset of bubble growth.

#### 4.2 Morphology of produced composites

A selection of produced composites demonstrating the effect of varied cavitation intensity are shown next. Every processing parameter affects the dispersion of particles, including the melting temperature, solidification rate, composition and surface properties of the reinforcement, the ambient atmosphere and the presence of solutes, even in low concentrations. For this reason, a certain degree of variance can be expected even for the same reinforcement-matrix system. However, when comparing the effect of different cavitation intensities in a specific particle-matrix pair, the processing parameters are kept the same within the possible limits.

Micrographs of Fe/TiC composites made without and with cavitation treatment are shown in Fig. 4 (a) and (b), respectively. The sample produced by simple melting exhibits a significant agglomeration of the Ti phase, shown in the left side of the light microscopy (LM) micrograph in (a). These clusters range from 200  $\mu\text{m}$  to 1 mm in diameter and appear at the edges of the composite. Most likely, as there is no cavitation, the ceramic phase is wetted relatively badly by the iron melt, providing conditions for the formation of agglomerates. These are then pushed to the side surfaces during the solidification. EDS mapping of an enlarged cluster (right side of (a), top) confirms the large amount of Ti being lost due to particle bundling. On the right part of Fig. 4 (a) LM micrograph, a typical example of matrix overview is presented. The image reveals that no large clusters exist within the matrix. Some porosity (larger round, black structures) can be seen. The back-scattered electron (BSE) image in the middle of (a) (bottom part) presents a typical higher magnification micrograph of a TiC phase within the iron matrix. The sample without any cavitation treatment consists of up to 8  $\mu\text{m}$  large TiC structures. A representative view of processing with a high intensity cavitation is shown in Fig. 4 (b). The melting is done with a  $B_{DC} = 3$  T strong magnetic field applied that, according to equation (5), corresponds to around 0.3 MPa pressure oscillation amplitude. Application of such intense cavitation treatment prevents clustering and the microstructure is refined as presented in the low magnification SEM image in the middle. A fraction of the added second phase consists of a few micrometers large TiC similar to the one marked with the black arrow. However, most of the matrix is filled with TiC smaller than 1  $\mu\text{m}$  (selected examples are marked with white arrows). A high magnification image of such fine TiC particle structures is presented on the right side. It is clear that the interspatial distance and distribution should be improved to achieve more uniform structures in the iron matrix. Nevertheless, a clear refinement of the TiC phase is obtained due to the high intensity cavitation treatment.

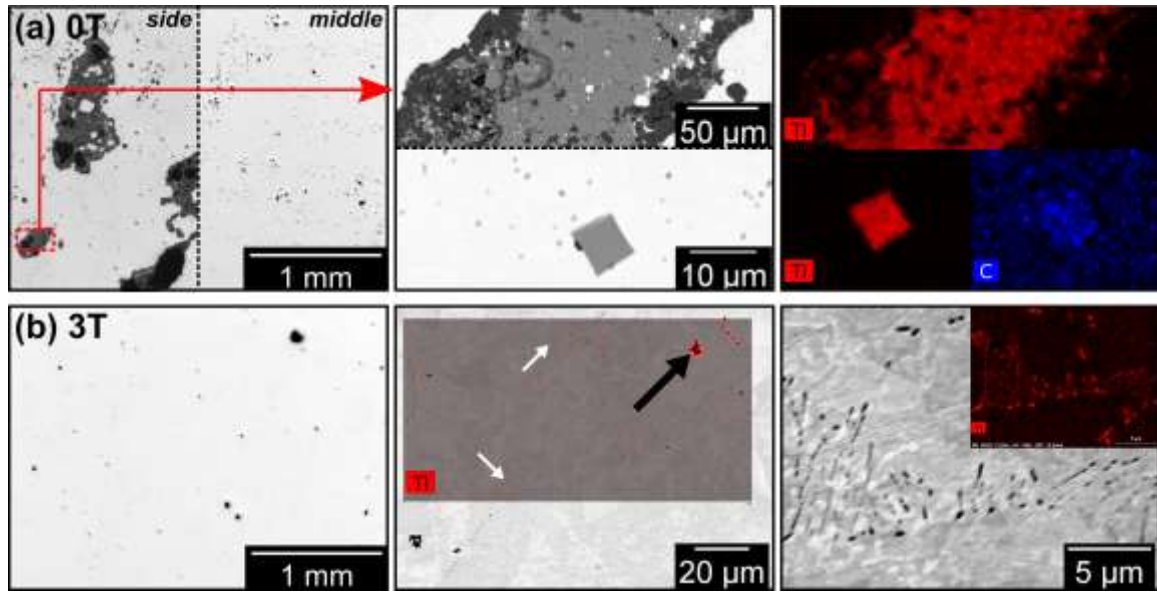


Fig. 4. Overview of the iron matrix with dispersed TiC particles with no cavitation (a) and with high cavitation intensity treatment (b) on the left (light microscopy; LM). Particle structures in detail in the middle (back-scattered electron contrast; BSE) and elemental analysis on the right (energy-dispersive X-ray spectroscopy; EDS). With no cavitation treatment, TiC agglomeration is found at the sides of sample (left of (a), left part). With cavitation, larger (black arrow) and refined (white arrows) TiC particles can be seen in the matrix (middle of (b)).

Fig. 5 presents a comparison of TiN particle dispersion in steel using weak cavitation treatment ( $B_{DC} = 0.5$  T corresponding to 52 kPa) in (a) and intensive cavitation treatment ( $B_{DC} = 3$  T corresponding to 0.3 MPa) in (b). Since good wettability of TiN by iron alloys has been demonstrated before by Amadeh et al. (2001), even with a low intensity cavitation treatment the particles are in the bulk of the matrix as expected. However, the particles tend to agglomerate in micron sized clusters. Additionally, larger clusters in sizes of 300  $\mu\text{m}$  can be found as presented at the top part of LM image in (a). A higher magnification of this cluster is shown in the middle with EDS mapping on the right of (a), respectively. Such agglomeration limits the fraction of the distributed reinforcement in the matrix. A particle-free region (secondary phase is in a dark contrast with the matrix) is shown at the bottom part of the LM image in (a). Higher magnification and EDS mapping demonstrate that, indeed, the TiN is not well distributed in the steel matrix. In contrast, much finer structures can be observed in the case of processing with a high cavitation intensity. The LM image of Fig. 5 (b) shows that the matrix is more refined in comparison with Fig. 5 (a), i.e. the clustering is substantially lowered. The magnified BSE micrograph in the middle demonstrates that the size of the TiN phase is reduced. Most importantly, the interspatial distance as well as distribution within the matrix is greatly improved. With a high cavitation intensity treatment, the TiN phase is better dispersed and in a size range of 1–5  $\mu\text{m}$ . Weak cavitation is clearly not sufficient for improvement of the composite microstructure. It must be noted that the elongated light gray structures visible in (b) are high in sulfur which also exists in (a) in a similar amount. However, this is left out of the EDS mapping for the sake of clarity.

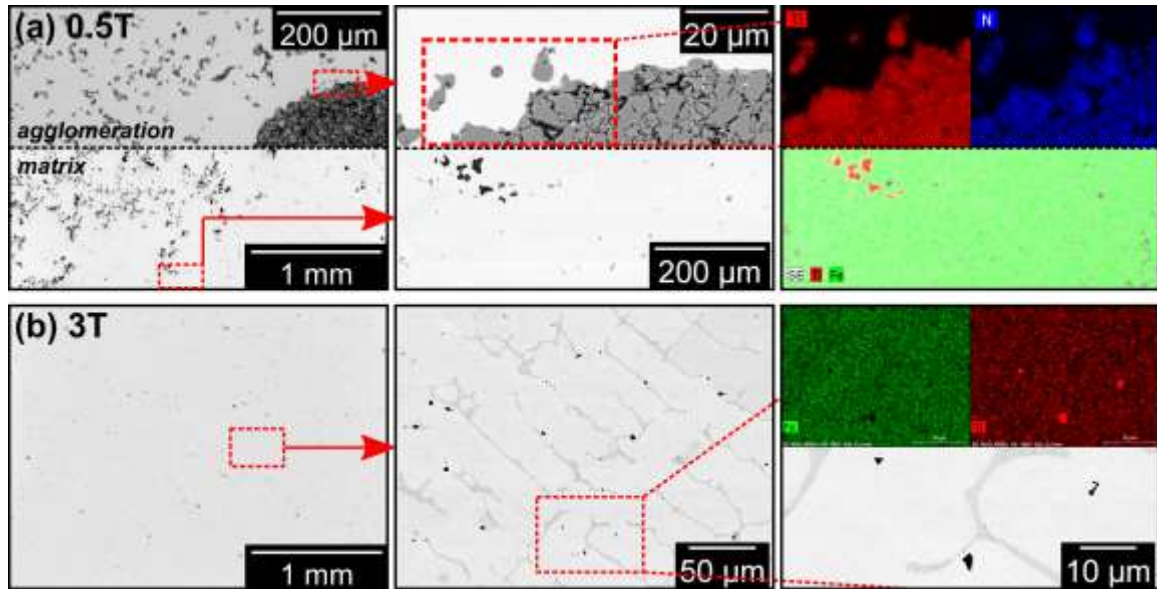


Fig. 5. Overview of the steel matrix with dispersed TiN particles with low (a) and high (b) cavitation intensity treatment on the left (LM). Matrix in detail in the middle (BSE contrast) and elemental analysis on the right (EDS). With weak cavitation, large agglomerates are found in the matrix, while other parts are particle-free (top and bottom of (a), respectively).

Micrographs of Fe/TiB<sub>2</sub> composite processed without and with high intensity cavitation treatment are shown in Fig. 6 (a) and (b), respectively. Without cavitation treatment two distinct phases of Ti exist. Firstly, some of the TiB<sub>2</sub> is stable inside the iron matrix. However, clusters tend to form and a typical agglomerate is demonstrated in the SEM micrograph in the middle of (a) (high contrast Ti signal in EDS overlay). Secondly, a distinct grain structure comprised of Ti is also present (low contrast Ti signal in EDS overlay). One such grain boundary is enlarged at the right side of Fig. 6 (a). However, the exact composition of the structure is not determinable by EDS. Formation of Ti rich grain boundaries and clusters limits the dispersion of the reinforcement phase within the matrix. Typically, almost no TiB<sub>2</sub> can be found in the iron matrix. Contrary, an improved dispersion is achieved with a high cavitation intensity. Similar to TiC and TiN processing, the melting is done in a  $B_{DC} = 3$  T high magnetic field. Overview of the matrix on the left side of (b) presents similar grain structures as in the case without cavitation treatment. While the grain size is apparently similar in both cases, the grain boundaries are typically thinner when cavitation is applied. Another important difference is the prevention of clustering. Similar to Fe/TiC, this increases the TiB<sub>2</sub> fraction within the matrix. While the grain boundaries are still formed from Ti, the grains are filled with well dispersed reinforcements of sizes smaller than 1 μm (SEM micrograph with EDS overlay in Fig. 6 (b) middle). A higher magnification of these particulates are shown on the right side of (b).

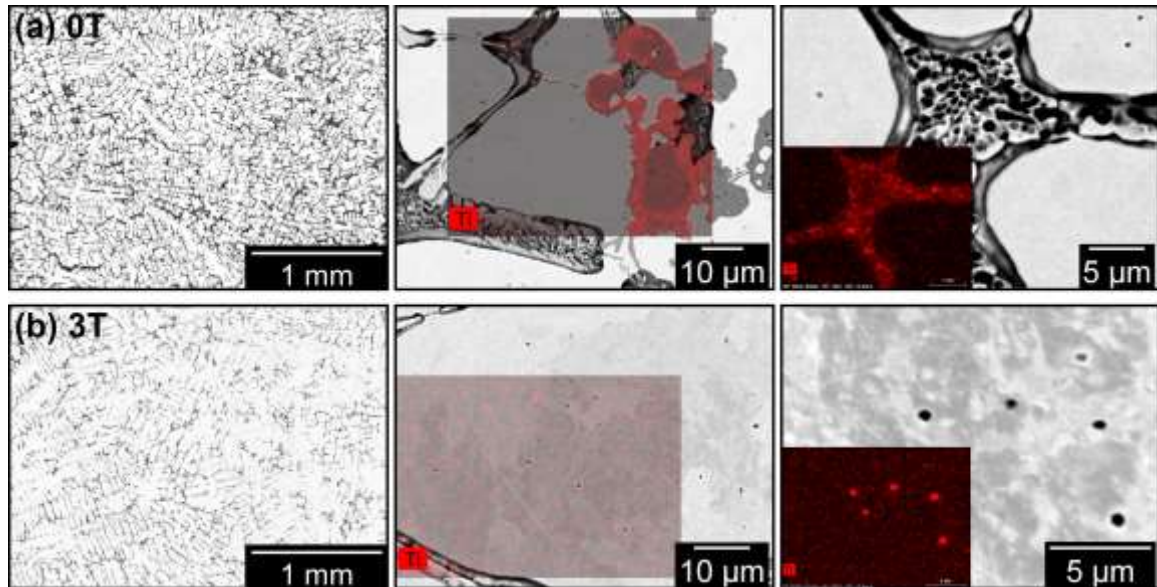


Fig. 6. Overview of the iron matrix with dispersed  $\text{TiB}_2$  particles with no cavitation (a) and with high cavitation intensity treatment (b) on the left (LM). Magnification of grain structures in the middle (BSE contrast; EDS overlay) and higher magnification of structures on the right (BSE contrast; EDS in the corner). Cavitation treatment provides improved  $\text{TiB}_2$  dispersion and refinement in the iron matrix.

Fig. 7 demonstrates  $\text{TiB}_2$  particle dispersion in steel without cavitation in (a) and with very high intensity cavitation processing in (b). As presented in the overview on the left side of Fig. 7 (a), without cavitation strong agglomeration of the reinforcement phase occurs. Clusters of up to  $200 \mu\text{m}$  can be found throughout the middle of the matrix. The high magnification BSE image in the middle displays enlarged clusters with Ti EDS overlay. Moreover, few individual particulates can be found in the matrix, as shown in an example on the right side of (a). Yet, these only make a small fraction of the reinforcement phase since clustering is preferential. A clearly improved matrix is obtained when processing is done in a  $B_{DC} = 8 \text{ T}$  strong magnetic field (corresponding to  $0.83 \text{ MPa}$  pressure oscillation amplitude). In a typical overview on the left side of Fig. 7 (b) no large particulate clustering can be seen. Applying  $8 \text{ T}$  magnetic field prevents the agglomeration and clearly disperses the  $\text{TiB}_2$  phase in the matrix as presented in the BSE micrograph in the middle. EDS mapping of the observable structures (Ti phase, Fe matrix, Cr rich structures and S inclusions) is shown on the right side. While much higher intensity cavitation has been applied in this particular case, the size of the  $\text{TiB}_2$  in steel is larger than the sizes observable in an iron matrix (also in case of other reinforcement-matrix pairs). Evidently, cavitation can act as a tool for distributing the reinforcement phase in the matrix, but material compatibility has to be taken into account as well. Nevertheless, a clear difference of particle dispersion can be seen and an improvement of the steel microstructure due to high intensity cavitation treatment is apparent.

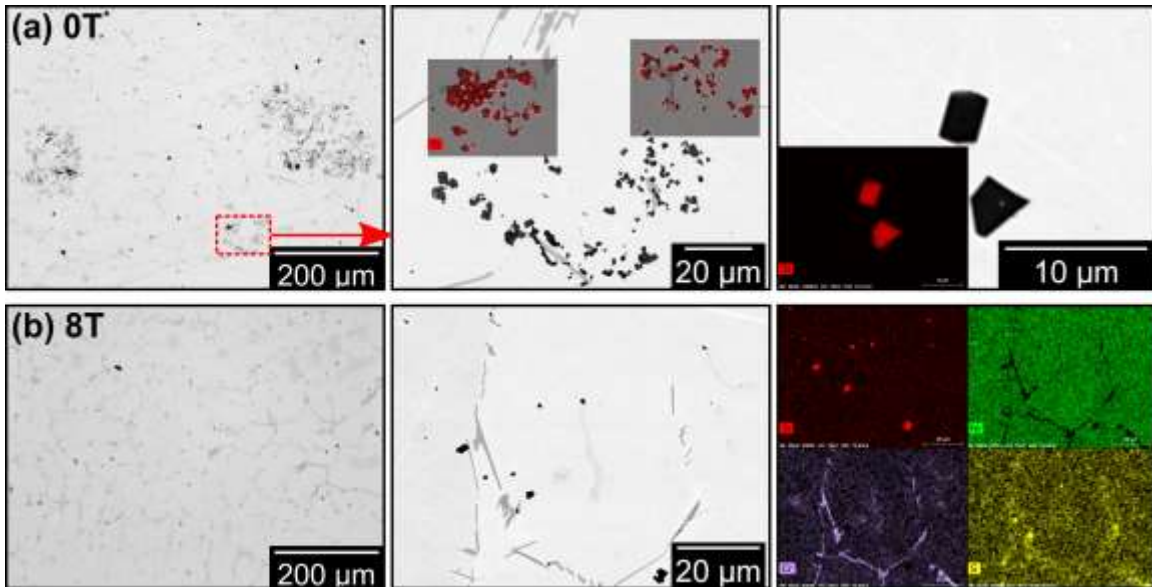


Fig. 7. Overview of the steel matrix with dispersed  $\text{TiB}_2$  particles with no cavitation (a) and with very high intensity cavitation treatment (b) on the left (LM). Particle structures in detail in the middle (BSE contrast). On the right side of (a) typical single particulates are presented. On the right side of (b) elemental analysis of the structures in the middle are shown.

## 5 Conclusions

The experiments described in this paper allow to effectively summarize the potential of contactless cavitation generation in high-temperature melts, as well as its possible shortcomings. The principle of contactless cavitation generated by electromagnetic forces using the floating-zone method is shown to be a feasible approach for treating steel and iron. The sound emitted by many collapsing bubbles has been recorded, and the characteristic frequencies related to cavitation, i.e. sub- and ultraharmonics, are clearly distinguishable.

The set-up is designed to reach the theoretically necessary oscillating pressure amplitude for the cavitation onset defined by the Blake threshold. However, the presence of readily available cavitation nuclei in the form of different impurities, dissolved gas and added particles significantly lowers the required value. This allows to use much weaker magnetic fields. It has been demonstrated that the DC magnetic fields do not have to be extreme: 0.8 T, which corresponds to an 83 kPa oscillating pressure amplitude, is sufficient to initiate cavitation in iron. However, the sporadic and subtle response to the pressure oscillations indicates that the cavitation does not reach its full potential when  $B_{DC} < 1$  T. The applied 14 kHz AC field frequency corresponds to a relatively large bubble resonance size. Thus, a higher alternating magnetic field  $b_{AC}$  frequency may have to be employed to ensure a stronger response by smaller cavities. The onset is also clearly affected by the generally unmeasurable quantity of cavitation nuclei, with a higher amount of impurities in the initial sample providing a stronger effect. This should be used as an advantage.

Improved particle dispersion and a reduction in precipitate size are clearly demonstrated as a result of the cavitation treatment, even if chemical reactions of some initial particulates cannot be excluded. The investigated ultra-high-temperature ceramics (borides, carbides and nitrides) can be well dispersed in iron and steel, and cavitation treatment reduces the agglomeration and

refines the reinforcement phase. However, a relatively strong DC field (in the order of 3 T, corresponding to a pressure oscillation amplitude of 0.3 MPa) has to be applied to achieve a significant effect. As the results presented cannot be directly generalized to other iron based alloys, it is clear that more material compatibility studies should be carried out with different steel grades. Examining iron compositions with different wettability-improving alloying elements would be beneficial as well. Such studies are recommended for further research. Additionally, the other benefits of ultrasonic processing, such as grain refinement and degassing, should be explored.

Nevertheless, considering the current advances in cryogen-free open-bore superconducting magnets, we see great potential for the proposed approach to be successfully used for highly reactive liquid metals at high temperatures – possibly even for steel composite production on an industrial scale.

### Acknowledgements

The financial support by the German Helmholtz Alliance “Liquid Metal Technologies – LIMTECH” is gratefully acknowledged. We also acknowledge the support of the HLD at HZDR, a member of the European Magnetic Field Laboratory (EMFL). The authors express their deepest gratitude to Stefan Findeisen, Thomas Gundrum and Falk Möller for their invaluable involvement during different stages of the experiments.

### References

- Amadeh, A., Manesh, S.H., Labbe, J.C., Laimeche, A., Quintard, P., 2001. Wettability and corrosion of TiN, TiN-BN and TiN-AlN by liquid steel. *Journal of the European Ceramic Society* 21, 277–282.  
[https://doi.org/10.1016/S0955-2219\(00\)00190-4](https://doi.org/10.1016/S0955-2219(00)00190-4)
- Bergner, F., Hilger, I., Virta, J., Lagerbom, J., Gerbeth, G., Connolly, S., Hong, Z., Grant, P.S., Weissgerber, T., 2016. Alternative fabrication routes toward oxide-dispersion-strengthened steels and model alloys. *Metallurgical and Materials Transactions A: Physical Metallurgy and Materials Science* 47, 5313–5324.  
<https://doi.org/10.1007/s11661-016-3616-2>
- Bojarevics, V., Djambazov, G.S., Pericleous, K.A., 2015. Contactless ultrasound generation in a crucible. *Metallurgical and Materials Transactions A: Physical Metallurgy and Materials Science* 46, 2884–2892.  
<https://doi.org/10.1007/s11661-015-2824-5>
- Bonnet, F., Daeschler, V., Petitgand, G., 2014. High modulus steels: new requirement of automotive market. How to take up challenge? *Canadian Metallurgical Quarterly* 53, 243–252.  
<https://doi.org/10.1179/1879139514Y.0000000144>
- Cramer, E., Lauterborn, W., 1982. Acoustic cavitation noise spectra. *Applied Scientific Research* 38, 209–214.  
<https://doi.org/10.1007/BF00385950>

Eskin, G.I., Eskin, D.G., 2014. Ultrasonic Treatment of Light Alloy Melts. CRC Press, Boca Raton, USA.

<https://doi.org/10.1201/b17270>

Fitzgerald, M.E., Griffing, V., Sullivan, J., 1956. Chemical effects of ultrasonics – “hot spot” chemistry. *The Journal of Chemical Physics* 25, 926–933.

<https://doi.org/10.1063/1.1743145>

Grants, I., Gerbeth, G., 2018. Stability of melt flow during magnetic sonication in a floating zone configuration. *Physical Review Fluids* 3, 1–14, art. no. 063902.

<https://doi.org/10.1103/PhysRevFluids.3.063902>

Grants, I., Gerbeth, G., Bojarevičs, A., 2015. Contactless magnetic excitation of acoustic cavitation in liquid metals. *Journal of Applied Physics* 117, art. no. 204901.

<https://doi.org/10.1063/1.4921164>

Henderson, H.B., Rios, O., Bryan, Z.L., Heitman, C.P.K., Ludtka, G.M., Ludtka, G.M., Melin, A.M., Manuel, M.V., 2014. Magneto-acoustic mixing technology: A novel method of processing metal-matrix nanocomposites. *Advanced Engineering Materials* 16, 1078–1082.

<https://doi.org/10.1002/adem.201300534>

Ilyichev, V.I., Koretz, V.L., Melnikov, N.P., 1989. Spectral characteristics of acoustic cavitation. *Ultrasonics* 27, 357–361.

[https://doi.org/10.1016/0041-624X\(89\)90034-6](https://doi.org/10.1016/0041-624X(89)90034-6)

Lan, J., Yang, Y., Li, X., 2004. Microstructure and microhardness of SiC nanoparticles reinforced magnesium composites fabricated by ultrasonic method. *Materials Science and Engineering A* 386, 284–290.

<https://doi.org/10.1016/j.msea.2004.07.024>

Leighton, T., 1994. The Acoustic Bubble. Academic Press, London, UK.

<https://doi.org/10.1016/B978-0-12-441920-9.X5001-9>

Li, Z., Xu, Z., Ma, L., Wang, S., Liu, X., Yan, J., 2019. Cavitation at filler metal/substrate interface during ultrasonic-assisted soldering. Part II: Cavitation erosion effect. *Ultrasonics Sonochemistry* 50, 278–288.

<https://doi.org/10.1016/j.ultsonch.2018.09.027>

Liu, X., Jia, S., Nastac, L., 2014. Ultrasonic cavitation-assisted molten metal processing of cast A356-nanocomposites. *International Journal of Metalcasting* 8, 51–57.

<https://doi.org/10.1007/BF03355591>

Ramqvist, L., 1965. Wetting of metallic carbides by liquid copper, nickel, cobalt and iron.

International Journal of Powder Metallurgy 1.

Springer, H., Fernandez, R.A., Duarte, M.J., Kostka, A., Raabe, D., 2015. Microstructure refinement for high modulus in-situ metal matrix composite steels via controlled solidification of the system Fe-TiB<sub>2</sub>. *Acta Materialia* 96, 47–56.

<https://doi.org/10.1016/j.actamat.2015.06.017>

Suslick, K.S., Didenko, Y., Fang, M.M., Hyeon, T., Kolbeck, K.J., McNamara, W. B., Mdleleni, M.M., Wong, M., 1999. Acoustic cavitation and its chemical consequences. *Philosophical Transactions of the Royal Society A: Mathematical, Physical and Engineering Sciences* 357, 335–353.

<https://doi.org/10.1098/rsta.1999.0330>

Terry, B.S., Chinyamakobvu, O.S., 1992a. Dispersion and reaction of TiB<sub>2</sub> in liquid iron alloys. *Materials Science and Technology* 8, 491–499.

<https://doi.org/10.1179/mst.1992.8.6.491>

Terry, B.S., Chinyamakobvu, O.S., 1992b. Dispersion and reaction of TiC in liquid iron alloys. *Materials Science and Technology* 8, 399–405.

<https://doi.org/10.1179/mst.1992.8.5.399>

Tzanakis, I., Eskin, D.G., Georgoulas, A., Fytanidis, D.K., 2014. Incubation pit analysis and calculation of the hydrodynamic impact pressure from the implosion of an acoustic cavitation bubble. *Ultrasonics Sonochemistry* 21, 866–878.

<https://doi.org/10.1016/j.ulsonch.2013.10.003>

Tzanakis, I., Lebon, G.S.B., Eskin, D.G., Pericleous, K.A., 2016. Characterisation of the ultrasonic acoustic spectrum and pressure field in aluminium melt with an advanced cavitometer. *Journal of Materials Processing Technology* 229, 582–586.

<https://doi.org/10.1016/j.jmatprotec.2015.10.009>

Ukai, S., Fujiwara, M., 2002. Perspective of ODS alloys application in nuclear environments. *Journal of Nuclear Materials* 307-311, 749–757.

[https://doi.org/10.1016/S0022-3115\(02\)01043-7](https://doi.org/10.1016/S0022-3115(02)01043-7)

Vivès, C., 1996. Crystallization of aluminium alloys in the presence of cavitation phenomena induced by a vibrating electromagnetic pressure. *Journal of Crystal Growth* 158, 118–127.

[https://doi.org/10.1016/0022-0248\(95\)00344-4](https://doi.org/10.1016/0022-0248(95)00344-4)

Wang, C., Gao, H., Dai, Y., Ruan, X., Shen, J., Wang, J., Sun, B., 2010. In-situ technique for synthesizing Fe-TiN composites. *Journal of Alloys and Compounds* 490, L9–L11.

<https://doi.org/10.1016/j.jallcom.2009.09.178>

Yuan, D., Yang, X., Wu, S., Lü, S., Hu, K., 2019. Development of high strength and toughness

nano-SiCp/A356 composites with ultrasonic vibration and squeeze casting. Journal of Materials Processing Technology 269, 1–9.

<https://doi.org/10.1016/j.jmatprotec.2019.01.021>